ORIGINAL PAPER

Mathematical modeling of an NMR chemistry problem in ovarian cancer diagnostics

Dževad Belkić · Karen Belkić

Abstract   We use mathematical modeling via the fast Padé transform (FPT) with respect to a theoretically-designed problem based on time signals that are similar to NMR data as encoded from benign and malignant ovarian cyst fluid. The FPT reconstructed exactly all the input spectral parameters by using exceedingly small fractions of the full time signals both for those corresponding to the benign, as well as to the malignant case. The converged parametric results remained stable thereafter at longer signal lengths. The Padé absorption spectra yielded clear resolution of all the extracted physical metabolites. The capacity of the FPT to resolve and precisely quantify the physical resonances as encountered in benign versus malignant ovarian cystic fluid is demonstrated. The practical significance of such findings is enhanced by the avoidance of the time signals' exponential tail which is embedded in the background, leading to problems in quantification. Without any fitting or numerical integration of peak areas, the FPT reliably yields the metabolite concentrations of major importance for distinguishing benign from malignant ovarian lesions. Thus, the FPT provides distinct advantages relative to the standard Fourier methodology, which is also stable, but has a number of drawbacks. These include limited resolution capacity, as well as non-parametric estimation, so that only a shape spectrum is generated and post-processing is necessary via, e.g., fitting or numerical integrations which are not unique. The FPT is also distinguished from other competitive parametric methods, which are generally unstable as a function of signal length N at a fixed bandwidth and, therefore, are particularly unsuit-

Dž. Belkić (✉) · K. Belkić
Department of Oncology-Pathology, Karolinska Institute, Box 260, Stockholm 17176, Sweden
e-mail: Dzevad.Belkic@ki.se

K. Belkić
Institute for Prevention Research, University of Southern California, Keck School of Medicine,
Los Angeles, CA 91803, USA
e-mail: Karen.Belkic@ki.se

able to clinical data. We conclude that these advantages of the FPT could be of definite benefit for ovarian cancer diagnostics via NMR and that this line of investigation should continue with encoded data from benign and malignant ovarian tissue, in vitro and in vivo. This avenue is of clinical urgency for early ovarian cancer detection, a goal which is still elusive and achievement of which would confer a major survival benefit.

Keywords Ovarian cancer · Magnetic resonance spectroscopy · Time signals · Quantification · Fast Padé transform

Abbreviations

Ala	Alanine
au	Arbitrary units
Cho	Choline
COSY	2 dimensional correlated spectroscopy
Cr	Creatine
Crn	Creatinine
C_{met}	Metabolite concentration
C_{ref}	Reference concentration
CT	Computerized tomography
DFT	Discrete Fourier transform
DLP	Decimated linear predictor
DPA	Decimated Padé approximant
DSD	Decimated signal diagonalization
FFT	Fast Fourier transform
FID	Free induction decay
FPT	Fast Padé transform
Glc	Glucose
Gln	Glutamine
Iso	Isoleucine
HLSVD	Hankel-Lanczos Singular Value Decomposition
Lac	Lactate
Lys	Lysine
Met	Methionine
MR	Magnetic resonance
MRI	Magnetic resonance imaging
MRS	Magnetic resonance spectroscopy
MRSI	Magnetic resonance spectroscopic imaging
NMR	Nuclear magnetic resonance
PA	Padé approximant
PLCO Trial	Prostate, Lung, Colorectal and Ovarian Trial
ppm	Parts per million
SCS	Statistical classification strategy
SNR	Signal-to-noise ratio
ST	Shanks transform
Thr	Threonine
TVUS	Transvaginal ultrasound
Val	Valine

1 Introduction

As recently underscored [1], resolution enhancement and accurate quantification of encoded biomedical data are of key relevance to such important public health problems as timely cancer diagnostics and screening. Insufficient accuracy of all the algorithms that are commercially available and built into clinical scanners hampers progress, especially in diagnostic modalities based upon magnetic resonance spectroscopy (MRS) and spectroscopic imaging (MRSI). Mathematics play a decisive role for improving the information extraction provided by MRS and MRSI [1]. In the present paper, we will focus upon the potential advantages of more advanced data analytical methods, such as the fast Padé transform (FPT) applied to MRS as these could specifically impact upon timely detection of ovarian cancer, a crucial goal which is still elusive.

1.1 The importance of data analytical methods for MRS

1.1.1 Conventional methods for signal processing in MRS (both in vivo and in vitro)

Heretofore, in vivo and in vitro MRS have relied almost exclusively upon the conventional theoretical framework for data analysis in biomedical imaging, i.e., the fast Fourier transform (FFT), which is a mathematical procedure for converting the encoded time signal into a corresponding frequency representation. The FFT generally shows steady convergence with increasing signal length N at a fixed bandwidth (or equivalently, with increasing total acquisition time T), such that reasonable looking MR total shape spectra can usually be obtained for not so severely truncated time signals. In practice, either simulated or encoded time signals are truncated i.e., of finite lengths ($N < \infty$). However, only the infinite time signals ($N = \infty$) give the exact Fourier coefficients. The lack of infinitely long time signals is circumvented by resorting to processors with extrapolation features, such as the FPT. Due to its steady convergence, there are no major troublesome surprises for varying signal lengths in the FFT, whereas nearly all parametric estimators are unstable as a function of N, such that oscillations (spikes and other artificial spectral structures) appear before eventual convergence (if any) [2,3]. These latter spurious findings of parametric estimators are unacceptable in the clinical setting. Hence, the reliance upon the computationally stable FFT, at the price of giving up on quantification.

The FFT is a low-resolution shape estimator. Within the FFT, a complex-valued Fourier spectrum is defined by using only *a single polynomial*:

$$F = \frac{1}{N} \sum_{n=0}^{N-1} c_n \, e^{-2i\pi nk/N}, \quad 0 \le k \le N-1, \tag{1}$$

where the expansion coefficients $\{c_n\}$ are the time signal points. The FFT provides a shape spectrum with pre-assigned frequencies whose minimal separation is determined solely by the total acquisition time, $T = N\tau$, where N is the set of all the available signal points and τ is the sampling time (inverse of the chosen bandwidth). The FFT

spectrum is defined only at the Fourier grid points $\bar{\omega}_k = 2\pi k/T \, (0 \leq k \leq N-1)$, and does not exist at other frequencies [2]. In fact, the FFT yields only a stick spectrum, although this may not be apparent when viewing the plottings, since the adjacent tips of the sticks are artificially connected.

Due to this well-known Fourier limitation, the only way to improve resolution is to increase T in order to decrease the distance $2\pi/T$ between the grid points. This strategy is fruitless, because magnetic resonance (MR) time signals encoded in vivo using clinical scanners become corrupted with background noise at longer T. The envelopes of MR time signals decay exponentially and, thus, are also termed free induction decay (FID). Therefore, signal intensity is highest early in the encoding. For this reason, it is advantageous to encode time signals as rapidly as possible, i.e., to avoid long T when mainly noise will be measured. These are, in fact, two mutually exclusive requirements leading to a conundrum whereby within the FFT, attempts to improve resolution will result in poorer signal-to-noise ratio (SNR).

A further problem with the FFT is that its single polynomial can only be a linear transform, which therefore, imports noise from the measured time domain data to the theoretically analyzed frequency domain, further compromising SNR [2]. The FFT also lacks extrapolation capabilities that cannot be replaced by the customary zero filling or periodic extension.

Another critical limitation of the FFT is that it is exclusively a non-parametric estimator, thus providing only the total shape or envelope of spectral structures, *but without quantification*. With the FFT, peak parameters are subsequently extracted with post-processing via e.g., fitting or numerical quadratures of peak areas. The problem is that e.g., 2, 3 or more resonances can yield the same fit to a given structure, with no way to tell which of the applied fits is correct. Particularly troublesome are over-lapping resonances, and these are often of clinical importance [4]. In the literature, contradictory findings have arisen related to whether or not a certain metabolite was included in the original expansion basis set for fitting [5,6].

Besides the fact that fitting is non-unique, vital information which it is actually contained in the FID is not obtained in this way, such that estimates for position, width, height and phase of resonances can be biased, despite a deceptive decline in the assessed Kramer-Rao error bounds. This is due to the non-orthogonality of basis set elements used in fittings. Any change in one or more of the adjustable parameters could largely be compensated by independent alterations in the remaining parameters [3]. Furthermore, the starting values for the sought spectral parameters (complex frequencies and amplitudes) are needed for fitting algorithms. Since these initial values are unknown, one is obliged to guess. As expected, various guesses yield different sets of estimates for the retrieved spectral parameters. What actually happens is that different local minima are found, rather than the correct, global minimum. This indicates how unreliable all the usual least square fitting routines are. The critical clinical information for cancer diagnostics is the extraction of the true concentrations of MR-detectable metabolites. These can only be accurately computed if the spectral parameters are reliably reconstructed with an intrinsic and robust error analysis.

1.1.2 Recent advances in signal processing methods: the fast Padé transform

Recent mathematical advances in signal processing via the FPT offer a distinct possibility to overcome many of the conventional limitations that are relevant to MR-based diagnostics. The FPT is a frequency-dependent, non-linear rational polynomial approximation P_L/Q_K (non-diagonal) or P_K/Q_K (diagonal) of the exact Maclaurin series with the encoded raw time signal points $\{c_n\}$ as the expansion coefficients. This polynomial quotient, as a rational function of angular frequency ω, is known as the Padé approximant (PA). The PA has alternatively been called the fast Padé transform for signal processing [2,7]. While the term "approximant" is typically used in numerical analysis, the word "transform" is deemed more appropriate for applications of the PA in signal processing. We thereby highlight a special feature of the PA in signal processing, i.e., the possibility of obtaining the shape spectrum from a time signal via non-parametric transformation reminiscent of the FFT. The Padé non-parametric estimation is performed by evaluating the polynomial quotient, e.g., P_{K-1}/Q_K or P_K/Q_K without ever searching for any of the spectral parameters, i.e., the complex-valued nodal/parent frequencies $\{\omega_k\}$ and the corresponding amplitudes $\{d_k\}$. In contrast, e.g., the Hankel-Lanczos Singular Value Decomposition (HLSVD) [8] computes the shape spectrum exclusively by first obtaining the peak parameters $\{\omega_k, d_k\}$. The FPT computes the ansatz spectrum $(1/N)\sum_{n=0}^{N-1} c_n z^{-n}$, which is a truncated version of the mentioned Maclaurin series (or equivalently, the truncated causal z-transform, or the truncated Green's function), via the unique ratio of two polynomials, e.g., in the para-diagonal form valid at any real or complex frequency ω:

$$F(z^{-1}) = \frac{1}{N}\sum_{n=0}^{N-1} c_n z^{-n} \tag{2}$$

$$F(z^{-1}) \approx R^-(z^{-1}), \quad R^-(z^{-1}) \equiv \frac{P_{K-1}^-(z^{-1})}{Q_K^-(z^{-1})} = \frac{\sum_{r=0}^{K-1} p_r^- z^{-r}}{\sum_{s=0}^{K} q_s^- z^{-s}}. \tag{3}$$

Here, z is a complex harmonic variable, $z = e^{i\omega\tau}$. The polynomial coefficients $\{p_r^-, q_s^-\}$ are extracted uniquely from the system of linear equations deduced from the matching condition $Q_K^- F = P_{K-1}^-$ by equating the coefficients of the same powers of z^{-1}. The Maclaurin expansion of $R^-(z^{-1})$ in terms of powers of z^{-1} is convergent outside the unit circle $|z| > 1$. Nevertheless, as a rational function, $R^-(z^{-1})$ is defined by analytical continuation (Cauchy) everywhere in the entire complex z- plane ($|z| < 1$, $|z| > 1$ except at $z = 0$ and $z = 1$). This is in sharp contrast to the original polynomial $F(z^{-1})$, which also converges for $|z| > 1$, but does not exist at all inside the unit circle $|z| < 1$. Due to the relation $F(z^{-1}) \approx R^-(z^{-1})$ from Eq. 3, the first $2K - 1$ expansion coefficients of the Maclaurin development of $R^-(z^{-1})$ and $F(z^{-1})$ are in exact agreement, i.e., $F(z^{-1}) - R^-(z^{-1}) = \mathcal{O}(z^{-2K+1})$. Here, the symbol $\mathcal{O}$ denotes the remainder which is a series containing the terms $z^{-2K+m}(m = 1, 2, 3, \ldots)$.

Function $F(z^{-1})$ should not be confused with the discrete Fourier transform (DFT). Namely, Eq. 2 will reduce to the DFT (which is an array $\{F_k\}$), only in a very special case by restricting z to the Fourier mesh $z = \bar{z}_k \equiv \exp(2\pi\, ik/N)$:

$$F_k \equiv F(\bar{z}_k^{-1}) = \frac{1}{N} \sum_{n=0}^{N-1} c_n e^{-2i\pi n\, k/N}, \quad 0 \le k \le N - 1, \tag{4}$$

as in Eq. 1. For the same input function $F(z^{-1})$, there is another equivalent variant of the FPT whose e.g., para-diagonal form also represents a polynomial quotient, but this time in terms of variable z:

$$F(z^{-1}) \approx R^+(z), \quad R^+(z) \equiv \frac{P_{K-1}^+(z)}{Q_K^+(z)} = \frac{\sum_{r=1}^{K-1} p_r^+ z^r}{\sum_{s=0}^{K} q_s^+ z^s} \tag{5}$$

The convergence region of $R^+(z)$ is inside the unit circle, $|z| < 1$. There is an important difference in the first expansion coefficients of the numerator polynomials P_{K-1}^- and P_{K-1}^+, since $p_0^- \ne 0$ and $p_0^+ \equiv 0$ as per Eqs. 3 and 5, respectively [2,7,9]. By the argument of analytical continuation (Cauchy), the rational polynomial from Eq. 5 is also defined in the whole complex z-plane ($|z| < 1$, $|z| > 1$ except at $z = 1$ and $z = \infty$). The two variants of the FPT defined inside ($|z| < 1$) and outside ($|z| > 1$) the unit circle will hereafter be denoted by the acronyms FPT$^{(+)}$ and FPT$^{(-)}$, respectively. In the present study, most of the analysis refers to the FPT$^{(-)}$. Therefore, whenever there is no chance for confusion, the label FPT$^{(-)}$ will be abridged to FPT. Similarly, unless otherwise indicated, we shall write $P_L^-(z^{-1}) \equiv P_L(z^{-1})$ and $Q_K^-(z^{-1}) \equiv Q_K(z^{-1})$.

An important characteristic of the FPT is its uniqueness. This means that for the two fixed integers L and K, there can be *one and only one* rational polynomial representation of the same input function $F(z^{-1})$. This, in turn, implies that the two Padé spectra $R^+(z)$ and $R^-(z^{-1})$, having the initial complementary convergence regions $|z| < 1$ and $|z| > 1$, respectively, must fully coincide with each other after convergence has been reached independently by the FPT$^{(+)}$ and the FPT$^{(-)}$. For noiseless synthesized time signals, given to machine accuracy, this is indeed the case in the exact sense ($R^+ = R^-$) [10]. The approximation, $R^+ \approx R^-$, is satisfied to within the level of the background noise after exhausting the full signal length [2,10] for noise-corrupted FID curves, both simulated and measured.

1.1.2.2 Determination of the exact number of resonances including those that overlap.

1.1.2.2.1 Use of the Hankel Matrix in the Time Domain: The encoded time signal contains the true information about the exact number K of resonances. Therefore, K is extractable from the data $\{c_n\}$ without guessing. This is in clear contradistinction to all the processors used in MR-based data analyses. To obtain K, the FPT is applied directly to the time signal stored as the Hankel or data matrix, $H_K(c_n)$. The FPT exists if, in the time domain, the equivalent Shanks transform (ST) of order K is zero, i.e., $e_K(c_n) = 0$ [2]. The ST of order K, $e_K(c_n)$, is proportional to the ratio of the two

Hankel determinants:

$$e_K(c_n) \propto \frac{H_{K+1}(c_n)}{H_K(c_n)}. \tag{6}$$

Therefore, the ST and the equivalent FPT are defined if the following two conditions are simultaneously fulfilled:

$$H_K(c_n) \neq 0, \quad H_{K+1}(c_n) = 0. \tag{7}$$

Hereafter, each signal point c_n is a sum of K damped complex exponentials $\exp(i\omega_k\tau)$ with the coefficients that represent stationary (d_k) and/or time-dependent ($d_{k,n}$) amplitudes. In the latter case, the amplitude $d_{k,n}$ is a polynomial of degree equal to the multiplicity of the fundamental frequency ω_k. In other words, the signature for the given signal to have K resonances is determined by verifying that both conditions in Eq. 7 are simultaneously satisfied. Moreover, the condition $H_{K+1}(c_n) = 0$ can be enlarged to encompass $H_{K+p}(c_n) = 0 (p = 1, 2, 3, \ldots)$. This has been shown to translate into the physically expected and plausible statement $d_{K+p} = 0 (p = 1, 2, 3, \ldots)$ [2,10].

In practice, to verify Eq. 7, the sequence of Hankel determinants of increasing order $\{H_m(c_n)\}$ ($m = 1, 2, \ldots$) is computed recursively [2]. The first integer $m' = m$ at which Eq. 7 is satisfied gives the total number of resonances, $K = m'$. Here, one should bear in mind that any metabolite, being a molecule, can have more than one resonance. Alternatively, the sequence $\{e_m(c_n)\}(m = 1, 2, \ldots)$ is computed via the Wynn recursion to detect $e_{m'}(c_n) = 0$ which then yields the sought $K = m'$. It has been shown in Ref. [2] that these two equivalent procedures for obtaining K exactly from the time signal $\{c_n\}$ are fully applicable to MRS data. This conceptual strategy is verified to work as per theory for synthesised, realistic time signals by exactly reconstructing any given number K of resonances [10].

1.1.2.2.2 Use of the Froissart doublets in the frequency domain: The FPT can determine K even without checking the two conditions in Eq. 7. This is done by computing a sequence of the Padé shape spectra $\{P_m/Q_m\}(m = 1, 2, 3, \ldots)$ in a frequency range of interest, say 0.5 ppm–5.5 ppm, as in the present study. Here, the fingerprint of detection of the exact number K of resonances is the attainment of the stabilization value $m = m'$ after which a saturation is systematically maintained by observing that $P_{m'+q}/Q_{m'+q} = P_{m'}/Q_{m'}(q = 1, 2, 3, \ldots)$. This critical transition ($m = m'$) yields the sought K as $K = m'$, and this is verified to work in practice with MRS signals [11]. This is the concept of Froissart doublets, or equivalently, pole-zero cancellations [10–12]. Such a cancellation in the Padé polynomial quotients $P_{K-1}^\pm/Q_K^\pm$ is due to the equality of the poles ($z_k^\pm$) and zeros ($\tilde{z}_k^\pm$):

$$z_k^\pm = \tilde{z}_k^\pm, \tag{8}$$

where $z_k^\pm \equiv z_k^{\pm 1}$ and $\tilde{z}_k^\pm \equiv \tilde{z}_k^{\pm 1}$. Hereafter, the roots of the characteristic equations $Q_K^\pm(z^{\pm 1}) = 0$ and $P_{K-1}^\pm(z^{\pm 1}) = 0$ are denoted by $z_k^{\pm 1}$ and $\tilde{z}_k^{\pm 1}$, respectively. The computation is carried out by gradually and systematically increasing the degree of the

Padé polynomials. As these degrees change, the reconstructed spectra fluctuate, until stabilization occurs. The value of the degree at which the desired level of accuracy is achieved, represents the sought exact number of resonances K. This constancy of the reconstructed values can be obtained, e.g., via the cannonical representation of the Padé polynomial quotients:

$$\frac{P_{K-1}^{\pm}(z^{\pm 1})}{Q_K^{\pm}(z^{\pm 1})} = \frac{p_{K-1}^{\pm}}{q_K^{\pm}} \frac{\prod_{k=1}^{K-1}(z^{\pm 1} - \tilde{z}_k^{\pm})}{\prod_{k'=1}^{K}(z^{\pm 1} - z_{k'}^{\pm})}. \tag{9}$$

This leads to cancellation of all the terms in the Padé numerator and denominator polynomials, when the computation is continued after the stabilized value of the order in the FPT has been attained:

$$\frac{P_{K-1+m}^{\pm}(z^{\pm 1})}{Q_{K+m}^{\pm}(z^{\pm 1})} = \frac{P_{K-1}^{\pm}(z^{\pm 1})}{Q_K^{\pm}(z^{\pm 1})}, \quad (m = 1, 2, 3, \ldots). \tag{10}$$

Whenever $z_k^{\pm} = \tilde{z}_k^{\pm}$, the amplitudes of the poles from Froissart doublets are exactly zero:

$$d_k^{\pm} = 0 \quad \text{for} \quad z_k^{\pm} = \tilde{z}_k^{\pm}. \tag{11}$$

This follows from the definition:

$$d_k^{\pm} = \frac{p_{K-1}^{\pm}}{q_K^{\pm}} \frac{\prod_{k'=1}^{K-1}(z_k^{\pm 1} - \tilde{z}_{k'}^{\pm})}{\prod_{k'=1, k' \neq k}^{K}(z_k^{\pm 1} - z_{k'}^{\pm})}. \tag{12}$$

Pole-zero cancellations occur as well whenever the computations detect multiplicities in $\{z_k^{\pm}\}$ even for an MR time signal whose spectrum is non-degenerate. When this occurs, the same spurious degeneracies also appear in $\{\tilde{z}_k^{\pm}\}$. This yields the degenerate Froissart doublets whose subsequent elimination via pole-zero cancellations provides the non-degenerate spectrum, as it should be for a spectrum which is defined as being comprised of pure Lorentzians.

The pole-zero cancellation also occurs, before detecting the true value of K for all the spurious poles that are cancelled by the corresponding spurious zeros. Thus, Froissart doublets provide a powerful means of determining whether a given reconstructed resonance is true or spurious. The concept of Froissart doublets can be used as a robust and reliable procedure for separating physical from non-physical (i.e., noise) information [11]. Finally, all the Froissart doublets are discarded, so that the reconstructed spectral parameters $\{\omega_k^{\pm}, d_k^{\pm}\}$ contain only genuine, physical information.

1.1.2.3 Computation of the complex frequencies and amplitudes by the FPT without fitting: Exact Quantification: Theoretical elaboration [2] and numerical validation [10,11] have been performed with respect to the computational algorithms by which the FPT provides the peak parameters needed to compute metabolite concentrations in

MRS. *This is done exactly without any fitting whatsoever and the solution is unique.* To obtain the peak parameters, the following equation is solved:

$$Q_K(z^{-1}) = 0. \tag{13}$$

This is known as the secular equation or the characteristic equation of the data (Hankel) matrix $\{c_{n+m}\}$. Since every polynomial of degree K has precisely K roots, Eq. 13 possesses K solutions $\{z_k^{-1}\}$ ($1 \leq k \leq K$):

$$z_k^{-1} = e^{-i\omega_k\tau}, \quad \omega_k = \frac{i}{\tau}\ln(z_k^{-1}). \tag{14}$$

As a non-linear numerical algorithm, rooting in Eq. 13 is usually unstable for higher values of K (e.g., $K > 200$). This problem can be avoided even without windowing, by solving the equivalent linear eigenproblem of an exceedingly sparse Hessenberg matrix of dimension $K \times K$ [2]. The eigenvalues of this latter matrix are, by definition, identical to the roots from Eq. 13. Insofar as windowing is used, as in Refs. [13–18], the dimensionality of the original problem can be reduced via band-limited decimation of the time signal. This yields the three novel estimators, the decimated Padé approximant (DPA), the decimated linear predictor (DLP) and the decimated signal diagonalization (DSD) that have been introduced in Refs. [13,14] to process time signals of arbitrarily long lengths.

After the K roots $\{z_k^{-1}\}$ of $Q_K(z^{-1})$ are found, the corresponding amplitudes $\{d_k\}$ are computed from the following explicit expression, given by the Cauchy residue of e.g., the paradiagonal polynomial ratio $P_{K-1}(z^{-1})/Q_K(z^{-1})$:

$$d_k = \frac{P_{K-1}(z_k^{-1})}{Q_K'(z_k^{-1})}, \tag{15}$$

where $Q_K'(z^{-1})$ is the first derivative of the denominator polynomial $Q_K(z^{-1})$:

$$Q_K'(z^{-1}) = \frac{d\,Q_K(z^{-1})}{dz^{-1}}. \tag{16}$$

The parametric complex Lorentzian spectrum is obtained from the Heaviside partial fraction expansion:

$$\frac{P_{K-1}(z^{-1})}{Q_K(z^{-1})} = \sum_{k=1}^{K} \frac{d_k}{z^{-1} - z_k^{-1}}. \tag{17}$$

Thereby, the FPT can yield the spectral parameters $\{\omega_k, d_k\}$ with minimal computational effort and maximal accuracy [10,11], where, the real, $\mathrm{Re}(f_k)$, and the imaginary, $\mathrm{Im}(f_k)$, part of f_k are the position and the width of the kth peak, while $|d_k|/\mathrm{Im}(f_k)$ and $Arg(d_k)$ are the corresponding height and phase, respectively, where $f_k = \omega_k/(2\pi)$.

Hereafter, the real and imaginary part of a general complex number u are denoted by Re (u) and Im (u), respectively.

It is once again emphasized that the FPT can find all the peak parameters of every physical resonance without ever using the Fourier spectrum, or any other spectrum at all, for that matter, as opposed to most fitting devices [19]. The Padé spectrum $\sum_{k=1}^{K} d_k/(z^{-1} - z_k^{-1})$ can afterwards be constructed for visualization purposes, in any of the desired modes (absorption, dispersion, magnitude, power, etc). In particular, the real part of the complex-valued spectrum $\sum_{k=1}^{K} d_k/\left(z^{-1} - z_k^{-1}\right)$ represents the absorption total shape spectrum Re $\left(\sum_{k=1}^{K} d_k/[z^{-1} - z_k^{-1}]\right)$, which is the sum of K absorption component shape spectra, Re $\left(d_k/[z^{-1} - z_k^{-1}]\right) (1 \le k \le K)$.

1.1.2.3.1 Quantification of overlapping resonances: The formulae from the sub-section (1.1.2.3) are valid for non-degenerate (purely Lorentzian) spectra, i.e., for all distinct roots $\{z_k^{-1}\}$ of Eq. 13 with $z_{k'}^{-1} \ne z_k^{-1} (k' \ne k)$. When any of these roots coincide with each other (degenerate roots—leading to overlapping resonances), the above formulae need to be modified. If, e.g., the kth root z_k^{-1} of $Q_K(z^{-1})$ has $M_k \le K$ multiplicity (i.e., it is repeated M_k times), then the Padé spectrum from Eq. 17 will be extended to have the following form:

$$\frac{P_{K-1}(z^{-1})}{Q_K(z^{-1})} = \sum_{k=1}^{J} \sum_{m_k=0}^{M_k} \frac{d_k^{(m_k)}}{(z^{-1} - z_k^{-1})^{m_k+1}}, \tag{18}$$

where $M_1 + M_2 + \cdots + M_J = K$. Then, the quantities $d_k^{(m_k)}$ become the new amplitudes that generalize Eq. 15 as:

$$d_k^{(m_k)} = \frac{P_{K-1}(z_k^{-1})}{Q_K^{(m_k)}(z_k^{-1})}, \tag{19}$$

where $Q_K^{(m)}(z^{-1})$ is the mth derivative of the denominator polynomial $Q_K(z^{-1})$,

$$Q_K^{(m)}(z^{-1}) = \left(\frac{d}{dz^{-1}}\right)^m Q_K(z^{-1}). \tag{20}$$

Moreover, with respect to the degenerate roots of Eq. 13, for the given N values of the signal points, one always obtains the unique quotient P_{K-1}/Q_K. The time signal $\{c_n\}$ associated with the physical Lorentzian spectrum from Eq. 17 with non-degenerate (distinct) roots $\{z_k^{-1}\}$ is given by:

$$c_n = \sum_{k=1}^{K} d_k e^{in\omega_k \tau}, \quad \text{Im}(\omega_k) > 0. \tag{21}$$

The time signal $\{c_n\}$ corresponding to the physical non-Lorentzian spectrum with degenerate (multiple) roots $\{z_k^{-1}\}$ is:

$$c_n = \sum_{k=1}^{J} d_{k,n} e^{in\omega_k \tau}, \quad d_{k,n} = \sum_{m_k=1}^{M_k} d_k^{(m_k)} (n\tau)^{m_k-1}, \quad \text{Im}(\omega_k) > 0. \qquad (22)$$

Here, it is seen that the non-stationary amplitude $d_{k,n}$ of the coincident/confluent resonances is a time-dependent polynomial of degree M_k which is the multiplicity of the root z_k^{-1} of $Q_K(z^{-1})$.

It is reemphasized that almost all fitting techniques use the Fourier spectrum to extract peak parameters for the sought resonances, whereas the FPT avoids fitting altogether. With the FPT, accurate quantification is achieved by extracting the spectral parameters of all the physical resonances (position, width, height, phase) directly from the encoded raw signal $\{c_n\}$. This leads to the Padé spectra according to the representations from Eqs. 17 and 18, for a Lorentzian and non-Lorentzian case, corresponding to FIDs given by (21) and (22), respectively [2,7,9,20].

By definition, all parametric estimators of exponentially damped time signals with stationary amplitudes $\{d_k\}$ yield the complex Lorentzian spectra given by $\sum_{k=1}^{K} d_k/(z^{-1} - z_k^{-1})$. This latter sum is, in fact, the Padé polynomial quotient $P_{K-1}^-(z^{-1})/Q_K^-(z^{-1})$ as indicated in Eq. 17. Thus, among all the parametric estimators, the FPT is, by definition, best suited to provide spectral analysis of MRS time signals if they are modeled by a linear combination of damped complex exponentials. This is also the case because the FPT is the exact filter for these FIDs containing attenuated complex exponentials (harmonics) with either constant or time-varying amplitudes (15) or (19) that yield the Lorentzian (17) or non-Lorentzian (18) spectrum, respectively [2]. Moreover, such modelling is also entirely realistic for carefully encoded FIDs from MRS/MRSI with adequate shimming and properly suppressed water by experimental procedures.

1.1.2.3.2 Accuracy of amplitude quantifications via the FPT: As seen from Eq. 15, in the FPT, the kth amplitude d_k depends *only* upon the kth root z_k^{-1}. For this reason, the d_k's found in the FPT are more accurate than those computed by, e.g., the HLSVD. The HLSVD computes the d_k's for the found set $\{z_m^{-1}\}$, by solving a system of linear equations from Eq. 21 for a given range of values of $n(0 \leq n \leq N - 1)$. As a consequence, all the frequencies from the set $\{z_m^{-1}\}$ ($m = 1, 2, 3, \ldots$) will contribute to each individual d_k. Thus, with the HLSVD any error in the values $\{z_m^{-1}\}$ (due either to spuriousness or insufficient accuracy in computation of otherwise physical frequencies) could severely compromise the reliability of the d_k's.

This problem does not occur in the FPT , since here each d_k is obtained separately from a single z_k^{-1} using the analytical formulae given by Eqs. 15 and 19 for a Lorentzian and a non-Lorentzian spectrum, respectively. The computational time is thereby diminished by about half, and, more importantly, this avoids another source of error from solving an additional system of linear equations used by the HLSVD.

All the methods for computing the d_k's must yield the same result for the common set of frequencies $\{\omega_k\}$. This uniqueness proof for the amplitudes/residues is given

in Ref. [2]. It is only natural, therefore, to use the simplest and the most accurate computation, as done in the FPT via the analytical expressions (15) and (19) for the amplitudes.

It should also be noted that the HLSVD is limited to exclusively pure Lorentzian spectra, whereas, as noted earlier, the FPT can treat both Lorentzian and non-Lorentzian spectra on the same footing according to Eqs. 17 and 18, respectively [2]. The fundamental frequencies $\{\omega_k\}$ must be the same in the FPT and the HLSVD. This is because the eigenroots of the characteristic polynomial (13) from the FPT are identical to the eigenvalues of the Hankel data matrix which is diagonalised in the HLSVD [2,8].

With the FPT , the shape spectrum can be obtained by using either the non-parametric or the parametric estimation from the two equivalent expressions $\left(\sum_{r=0}^{K-1} p_r z^{-r}\right)\Big/$ $\left(\sum_{s=0}^{K} q_s z^{-s}\right)$ or $\sum_{k=1}^{K} d_k \big/\left(z^{-1} - z_k^{-1}\right)$ where $2K = N$, respectively. Such estimations can be done at any frequency ω which is contained in $z = \exp(i\omega\tau)$. This is in sharp contrast with the FFT which can be computed only at the Fourier grid $z = \bar{z}_k = \exp(2i\pi\, k/N)$ as per definition of the DFT from Eq. 4.

1.1.2.4 Improvements in Resolution and SNR using the FPT   In the DFT from Eq. 4 and the ensuing FFT, the coefficients $\{\exp(-2i\pi n\, k/N)\}$ are independent of the c_n's , and this leads to a *linear* Fourier response function $F(\bar{z}_k^{-1})$ with no possibility for noise suppression, except for signal averaging. In other words, as mentioned, it is the linearity of the FFT which is responsible for transporting the whole and intact noise from the domain of measurement (time) to the domain of the theoretical analysis (frequency).

By contrast, in the FPT, the corresponding coefficients for transformation from the time to the frequency domain are *dependent* upon the time signal points $\{c_n\}$, and this yields a *non-linear* response functions $R^{\pm}(z^{\pm 1})$. The non-linearity of the FPT effectively permits noise suppression.

Furthermore, as is clear from Eq. 4, the FFT has a linear convergence $(1/N)$ with increased signal length N, while the convergence of FPT is quadratic ($\sim 1/N^2$) or exponential near the Froissart stability region [2,11]. This secures a rapid convergence with the implied resolution enhancement of the FPT relative to the FFT, especially at more severe truncations of the otherwise unavailable infinitely long time signal, or equivalently, at shorter acquisition times. Indeed, such expectations have been confirmed in Refs. [2,3,7,21] by detailed comparisons of the FPT and FFT from clinical ^{1}H-MRS data at 4T and 7T.

We will now turn our attention to the clinical problem of ovarian cancer, and explain how the advantages of the FPT might be of benefit to improved detection via MRS.

1.2 Ovarian cancer: the crucial and still elusive goal of early diagnosis

Worldwide, ovarian cancer is the seventh leading cause of death from cancer among women [22] and is the most common cause of death from gynecologic cancer in many developed countries [23]. In the year 2000 alone, over 100,000 women worldwide died from ovarian cancer [22]. Ovarian malignancies are diagnosed at a median age

of 58 years [24]. While strong family history of ovarian cancer and/or the presence of *BRCA*1 or *BRCA*2 mutations[1] are associated with an elevated risk, 90% of ovarian cancers occur in women who are not in an identifiable high-risk group [25].

Ovarian cancer is usually detected after spread beyond the true pelvis, when the prognosis is poor, whereas stage Ia disease has a 5-year survival rate well over 90%. Therefore, survival vitally depends upon early detection of ovarian cancer [26,27]. However, this is still beyond current reach with standard diagnostic methods [28].

While useful for follow-up of patients with established ovarian cancer, the tumor marker[2] CA-125 is neither sufficiently sensitive nor specific to improve early detection when used alone [29,30]. Small-scale studies examining genomic and proteomic patterns as possible complementary biomarkers for early ovarian cancer have shown promise [31–34]. However, further investigation is needed to determine whether these findings truly provide sufficient improvement in diagnostic accuracy to warrant their more widespread application for ovarian cancer screening [26,34,35].

Although sensitive, transvaginal ultrasound (TVUS) lacks adequate specificity to distinguish benign from malignant adnexal changes. The high rate of false positive findings with TVUS leads to many surgical procedures that do not find any malignancy [26]. There are several large-scale trials on-going to determine whether the combination of TVUS plus CA-125 could provide acceptable levels of diagnostic accuracy for ovarian cancer screening. This does not appear to be the case, however. For example, in the Prostate, Lung, Colorectal and Ovarian (PLCO) Trial involving nearly 40,000 women, the positive predictive value of abnormal TVUS plus CA-125 was only 23.5%. This meant that in order to find 26 cases of ovarian cancer (plus 3 other malignancies), 535 women underwent surgical exploration [36]. There are numerous deleterious consequences of such poor specificity. In the PLCO Trial study, e.g., false-positive findings were associated with significantly poorer adherence to the Trial, as well as with emotional distress [37]. Particularly because of the high false positive rates of the existing screening methods, the US Preventive Services Task Force [38] recommended against routine screening for ovarian cancer.

1.2.1 Results achieved with in vivo MR-based modalities for ovarian cancer diagnostics

The accuracy with which ovarian cancer is diagnosed has been enhanced by MR-based modalities. For example, the positive predictive value of TVUS can be improved by combination with other morphological imaging techniques, e.g., magnetic resonance imaging (MRI), as well as Doppler flow imaging, computerized tomography (CT). MRI is generally considered to be the most accurate for assessing adnexal masses prior to surgery, to distinguish benign from cancerous lesions and in some cases to make a specific diagnosis [38,39]. Comparing the three morphological imaging

---

[1] The *BRCA*1 and *BRCA*2 genes are presumed to act as tumor suppressors. Mutations which impair the function of either of these two genes can thereby interfere with this tumor suppression.

[2] CA-125 is a protein whose presence is often associated with ovarian cancer. However, it has poor sensitivity for early stage malignancy and is also non-specific, being present in other cancers, as well as several non-malignant conditions, including pregnancy.

modalities in a meta-analysis, MRI was found to be of greatest incremental value in identifying ovarian cancer when the nature of adnexal mass was considered indeterminate on TVUS [40]. However, even with contrast-enhanced MRI, which provided the best results, sixty of 241 (24.9%) false positive findings from initial TVUS were not recognized as benign lesions [41].

Moreover, it should be recalled that as opposed to CT, it is well-known that MRI and other MR-based diagnostic techniques entail no exposure to ionizing radiation. This could be of importance for groups at increased risk of ovarian cancer, for whom there is some (albeit not entirely conclusive) evidence that exposure to diagnostic medical radiation is associated with further elevation in risk [41,42].

While MRI has provided high spatial resolution to examine morphology, the need to assess beyond more than purely anatomic aspects, such as biochemistry and tissue physiology, required the development of functional techniques. As a non-invasive method providing metabolic information, MRS enables tissue characterization at a biochemical level, thus complementing MRI. MRS is also able to detect abnormalities that are invisible to MRI, because metabolic abnormalities often precede anatomical/morphological changes [28,43].

Thus far, there have been only a few investigations applying in vivo proton MRS to evaluate ovarian masses [44–47]. Altogether, some 18 malignant and 54 benign lesions of various histopathology, as well as one borderline cancerous adnexal mass have been examined in this way. Only a limited number of metabolites could be identified (choline at 3.2 parts per million (ppm), inverted lactate doublet at around 1.3 ppm, creatine at 3.0 ppm and lipid at 1.3 ppm, and their concentrations were estimated semi-quantitatively as strongly present or present versus absent. None of these metabolites clearly distinguished cancerous from benign lesions, such that the results are inconclusive. It is still technically difficult to encode good quality time signals due to motion artifacts from respiratory and peristaltic movements [44]. Because of the small size and motion of this organ, in vivo MRS is mired by problems of resolution and SNR.

1.2.2 In vitro MRS in ovarian cancer diagnostics

Substantially more investigation of malignant and benign ovarian lesions using MRS has been performed in vitro using high magnetic field strength and laboratory specimen processing techniques. These studies distinguish malignant and normal tissues in a better way, and offer some insights into molecular mechanisms.

Using peak amplitude ratios, Smith and Blandford [48] were able to differentiate normal and benign from borderline and malignant ovarian samples with 95% sensitivity and 86% specificity. They employed linear discriminant analysis training using leave-one-out (12 normal, 22 cancer) for analysis of 7 normal and 15 cancer specimens. The discriminating resonances were: 1.47 ppm (fatty acid), 1.68 ppm (lysine), 2.80 ppm (fatty acid), 2.97 ppm (creatine), 3.17 ppm (choline) and 3.34 ppm (taurine). Wallace et al. [50] evaluated 19 normal, 3 borderline, and 37 ovarian carcinomas, based upon peak amplitude ratios of the following resonances: 0.9 ppm (lipid methyl), 1.3 ppm (lipid methylene), 1.7 ppm (lysine and polyamines) and 3.2 ppm (choline). Normal/benign samples could be distinguished from borderline and malignant samples with a sensitivity of 95% and specificity of 86% [49].

Results from a study by Massouger et al. [50] of fluid samples from 9 malignant and 19 ovarian cysts also showed higher lactate, isoleucine, valine, methionine and alanine in the cancerous specimens, but again generally with wide, overlapping ranges. In addition, these authors found higher 3-hydroxybutyrate and pyruvic acid in the malignant cyst fluid. They note that rapid cellular metabolism will lead to elevated 3-hydroxybutyric acid. The high concentrations of branched chain amino acids (isoleucine, leucine, and valine) are seen as protein breakdown products due to necrosis and proteolysis. Also included in their study was an endometrioma, whose fluid showed much higher levels of isoleucine, valine, threonine, alanine, lysine, methionine, and glycine than did the malignant cysts.

A very detailed comparison of the spectroscopic features of ovarian cancer versus non-malignant cysts is provided by Boss et al. [51]. Ovarian cyst fluid samples were taken from 40 patients (12 with malignant and 28 with benign tumors). One dimensional in vitro MRS as well as two dimensional correlated spectroscopy (COSY) analyses were performed. There were numerous differences in metabolic concentrations between the cancerous and benign cysts. In their study, concentrations of isoleucine (1.02 ppm), valine (1.04 ppm), threonine (1.33 ppm), lactate (1.41 ppm), alanine (1.51 ppm), lysine (1.67–1.78 ppm), methionine (2.13 ppm), glutamine (2.42–2.52 ppm) as well as choline (3.19 ppm) were all significantly higher in the malignant samples, although no metabolites were found which provided absolute distinction between cancerous and non-cancerous cyst fluid.

Notwithstanding the important achievements of in vitro MRS for ovarian cancer diagnosis, there are still major problems that hamper more widespread application of MRS to this clinical area. These problems preclude a more definitive approach whereby the in vitro findings could be considered the "*gold standard*" with which MRS signals encoded in vivo from the ovary could be compared, and which might even surpass the accuracy of histopathology, as envisioned by Mountford et al. [52]. Gluch [53], e.g., comments on the statistical classification strategy (SCS) used in the above-described in vitro analyses. He raises the question of the suitability of this methodology for more complex pathological entities: "A classifier can more readily be developed when the likelihood of belonging to a class of either 'yes' or 'no', but when a tissue undergoes numerous stages in evolution from normal to malignant, SCS shows no superiority over conventional pathology" (p. 467). He notes that the high diagnostic accuracy is achieved by excluding the fuzzy samples (citing an example for which this was 27%). Concordant with the observations of Gluch [53], it should be noted that even in the study by Boss et al. [51], which provided, to date, the most extensive in vitro analysis of MRS signals from benign and malignant ovarian samples, the cited ranges for each of the metabolites were very wide and overlapping. From the vantage point of a clinician, Gluch [53] enumerates the limitations of ^{1}H MRS as a diagnostic tool in oncology. Among these were the lack of reliable in vitro data bases, lack of specificity of findings such as narrow lipid resonances, which can also be seen with necrosis, inflammation and other non-malignant processes. He points out that difficulties arise not so much in regards to the large lesion with suspicious imaging characteristics, but with respect to small or *in situ* lesions. It is precisely for these early stages of the disease when the most sensitive and specific diagnostic methods are needed the most. Gluch [54] notes that the "chance of missing a cancer of the order of only 1% would

translate into a significant medicolegal concern, and for this reason clinicians have to err on the side of caution. Substituting one doubtful test with another leads to no greater certainty in clinical decision making" (p. 467).

It should be emphasized that most of the estimates of metabolite concentrations, including those of Ref. [51], were based upon integrating the areas under the peaks in the Fourier absorption spectra. This procedure is vulnerable to subjectivity due to the uncertainty with lower and upper integration limits. Such a technique for reconstructing metabolite concentrations is particularly difficult with peak overlap ("spectral crowding"), which is known to create quantification problems [54]. Of particular note is that concentrations of adjacent resonances such as threonine (1.33 ppm), lactate (1.41 ppm) and alanine (1.51 ppm) and the nearly overlapping resonances isoleucine and valine in the region of 1.02–1.04 ppm appear to be of major importance for distinguishing benign and malignant ovarian specimens. This underscores the need for exact, unequivocal quantification not only of non-degenerate spectra with distinct roots, but also of those with degenerate roots, i.e., overlapping resonances. As elaborated earlier in this paper, the FPT would appear to be ideally suited to this task.

1.3 Aim of the present study

In the present study we examine the performance of the FPT applied to theoretically generated (synthesized or simulated) time signals that are reminiscent of in vitro MRS data as encoded from benign and malignant ovarian cyst fluid at a strong magnetic field $B_0 \approx 14.1$T in a 600 MHz NMR spectrometer [51]. These are viewed as the first steps in the process of determining whether the described features of the FPT could be of potential benefit for ovarian cancer diagnostics via MRS.

2 Results

We synthesized two FIDs of the type $c_n = \sum_{k=1}^{K} d_k e^{in\tau\omega_k}$ as in Eq. 21 via a sum of $K = 12$ damped complex exponentials $\exp(in\tau\omega_k)(1 \leq k \leq 12)$ with time-independent (stationary) amplitudes d_k. These time signals were subsequently quantified using the FPT, as described in [10,55].

2.1 Input data

For the benign case, we derived the input data for the spectral parameters from those reported for median concentrations C_{met} (expressed in µmol/l) of 12 metabolites that were characteristic of benign ovarian cyst fluid [51]. These median values were obtained from twenty-three patients with benign ovarian cysts collected by Boss et al. [51]. The input data are shown in Table 1.

Likewise, malignant concentrations correspond to the median values for malignant ovarian cysts from twelve patients [51], and these are used as the input data for the malignant case (Table 2).

Table 1 Input data from theoretically generated (synthesized) FIDs reminiscent of in vitro MRS data as encoded from benign ovarian cyst fluid [52]

Entry data (Benign)

k	Metabolite assignment	Re (f_k) (ppm)	Im (f_k) (ppm)	$|d_k|$ (au)	Concentration (μmol/L)
1.	Isoleucine (Iso)	1.020219	0.000818	0.003060	10
2.	Valine (Val)	1.040048	0.000821	0.034578	113
3.	Threonine (Thr)	1.330124	0.000822	0.027540	90
4.	Lactate (Lac)	1.410235	0.000828	0.758570	2479
5.	Alanine (Ala)	1.510318	0.000824	0.089657	293
6.	Lysine (Lys)	1.720125	0.000823	0.030906	101
7.	Methionine (Met)	2.130246	0.000819	0.002142	7
8.	Glutamine (Gln)	2.470118	0.000825	0.084149	275
9.	Creatine (Cr)	3.050039	0.000822	0.019278	63
10.	Creatinine (Crn)	3.130227	0.000821	0.020808	68
11.	Choline (Cho)	3.190136	0.000820	0.004590	15
12.	Glucose (Glc)	5.220345	0.000829	0.424419	1387

Hereafter, Re (f_k) denotes the chemical shift as the relative frequency in dimensionless units of parts per million (ppm) and au denotes arbitrary units

Table 2 Input data from theoretically generated (synthesized) FIDs reminiscent of in vitro MRS data as encoded from malignant ovarian cyst fluid [52]

Entry data (Malignant)

k	Metabolite assignment	Re (f_k) (ppm)	Im (f_k) (ppm)	$|d_k|$ (au)	Concentration (μmol/L)
1.	Isoleucine (Iso)	1.020219	0.000828	0.024174	79
2.	Valine (Val)	1.040048	0.000831	0.120869	395
3.	Threonine (Thr)	1.330124	0.000832	0.075887	248
4.	Lactate (Lac)	1.410235	0.000838	2.000000	6536
5.	Alanine (Ala)	1.510318	0.000834	0.179315	586
6.	Lysine (Lys)	1.720125	0.000833	0.149939	490
7.	Methionine (Met)	2.130246	0.000829	0.018972	62
8.	Glutamine (Gln)	2.470118	0.000835	0.253366	828
9.	Creatine (Cr)	3.050039	0.000832	0.020196	66
10.	Creatinine (Crn)	3.130227	0.000831	0.024174	79
11.	Choline (Cho)	3.190136	0.000830	0.012852	42
12.	Glucose (Glc)	5.220345	0.000839	0.079559	260

The FIDs from Ref. [51] were recorded with a static magnetic field strength $B_0 \approx$ 14.1T (Larmor frequency of 600 MHz) and a bandwidth of 6667 Hz. The inverse of this bandwidth is used for the sampling time τ in the presently synthesized FIDs. The total signal length N from Ref. [51] has been chosen so as to satisfy the Fourier resolving power $\Delta\omega_{min} = 2\pi/T$. In Ref. [51], use has been made of this latter relation for the chosen bandwidth 6667 Hz to aim at a spectral resolution $\Delta\omega = 0.02$ ppm, which should split apart isoleucine and valine as the two most tightly spaced metabolites. It then follows that the closest integer in the form 2^m for the FID length required in the FFT is $N = 2^{15} = 32768 = 32$ K (1K= 1024). With such a set-up, the FFT spectrum in Ref. [51] has been computed by zero-filling the two encoded FIDs each to 64 K. We

have verified (see sub-Sect. 2.2.2) that 32 K signal points augmented by 32 K zeros is the first FID length which simultaneously gives the converged absorption spectra and resolves all the metabolites in the Fourier absorption spectra. By contrast, as mentioned, the FPT resolution is not predetermined by $2\pi/T$ and, thus, shorter FID length could suffice. Therefore, we sampled our FIDs using only $N = 1024$ and, moreover, $N/16 = 64$ signal points were sufficient to solve the quantification problem with the resulting exact reconstruction (see sub-Sect. 2.2.1).

The input peak amplitudes were extracted from the tabulated data from Ref. [51] using the quotient $2C_{met}/C_{ref}$. Here, the reference concentration C_{ref} was taken to be the largest concentration from Ref. [51] (6536 μmol/L), namely the median lactate concentration in the malignant samples. The phases $\varphi_k (1 \leq k \leq 12)$ from d_k were all set to zero so that every amplitude d_k becomes real, $d_k = |d_k|$. The line-widths in Ref. [51] were estimated to be about 1 Hz. In our synthesized FIDs, the line-widths were allowed to have small variations within the interval $\{8.19, 8.39\} \times 10^{-4}$ ppm (these are labeled as Im (f_k) in the Tables).

2.2 Reconstructed data

2.2.1 Parametric data

Using the diagonal FPT to analyze the encoded FIDs, the coefficients $\{p_r, q_s\}$ of the polynomials P_K and Q_K were computed by solving the systems of linear equations deduced from definition (3), treating the product in $G_N(z^{-1}) * Q_K(z^{-1}) = P_{K-1}(z^{-1})$ as a convolution [10,11].

To extract the peak parameters, one solves the characteristic equation $Q_K(z^{-1}) = 0$, as in Eq. 13. This leads to K unique roots $z_k^{-1} (1 \leq k \leq K)$, so that the sought ω_k is deduced via $\omega_k = (i/\tau) \ln(z_k^{-1})$, as in Eq. 14.

The FPT extracts the parameters $\{\omega_k, d_k\}$ $(1 \leq k \leq K)$ of every physical resonance directly from the raw encoded FID. The kth metabolite concentration is computed from the reconstructed peak parameters (peak positions Re(ω_k), widths Im(ω_k) and the amplitudes d_k).[3] In the FPT, the kth amplitude d_k depends only upon the kth root z_k^{-1} and it is obtained analytically from the Cauchy residue theorem given in Sect. 1.1.2.3.

Peak area is proportional to the concentration of the metabolite, relative to a selected reference concentration (C_{ref}), which in this particular problem is 6536 μmol/L, the median lactate concentration in the malignant samples, which was the largest concentration from Ref. [51], as mentioned. Thus, the metabolite concentrations are computed simply as $[(6536 \mu mol/L)(d_k)]/2$.

Tables 3 and 4 show the reconstructed data at three signal lengths ($N/32 = 32$, $N/16 = 64$ and $N/8 = 128$) with the same bandwidth, for the benign and malignant cases, respectively. On the left set of columns of these two tables, it is seen that

---

[3] Recall that all the phases $\{\varphi_k\}(1 \leq k \leq K)$ were set to zero, so that the amplitudes are real.

Table 3 Reconstructed data at 3 signal lengths with 32, 64 and 128 FID points (data for benign)

| N/32 = 32 | | | | N/16 = 64 | | | | N/8 = 128 | | | | | |
Re (f_k) (ppm)	Im (f_k) (ppm)	|d_k| (au)	Concentration (μmol/L)	Re (f_k) (ppm)	Im (f_k) (ppm)	|d_k| (au)	Concentration (μmol/L)	Re (f_k) (ppm)	Im (f_k) (ppm)	|d_k| (au)	Concentration (μmol/L)	k	Metabolite assignment
–	–	–	–	1.020219	0.000818	0.003060	10	1.020219	0.000818	0.003060	10	1.	Isoleucine (Iso)
1.040033	0.001124	0.038143	125	1.040048	0.000821	0.034578	113	1.040048	0.000821	0.034578	113	2.	Valine(Val)
–	–	–	–	1.330124	0.000822	0.027540	90	1.330124	0.000822	0.027540	90	3.	Threonine (Thr)
1.409673	0.001117	0.796643	2603	1.410235	0.000828	0.758570	2479	1.410235	0.000828	0.758570	2479	4.	Lactate (Lac)
1.482370	0.005257	0.081645	267	1.510318	0.000824	0.089657	293	1.510318	0.000824	0.089657	293	5.	Alanine (Ala)
1.706966	0.009141	0.035360	116	1.720125	0.000823	0.030906	101	1.720125	0.000823	0.030906	101	6.	Lysine (Lys)
2.207406	0.216536	0.005435	18	2.130246	0.000819	0.002142	7	2.130246	0.000819	0.002142	7	7.	Methionine (Met)
2.470151	0.000826	0.082607	270	2.470118	0.000825	0.084149	275	2.470118	0.000825	0.084149	275	8.	Glutamine (Gln)
3.058390	0.001607	0.020043	66	3.050039	0.000822	0.019278	63	3.050039	0.000822	0.019278	63	9.	Creatine (Cr)
3.141312	0.002566	0.024686	81	3.130227	0.000821	0.020808	68	3.130227	0.000821	0.020808	68	10.	Creatinine (Crm)
–	–	–	–	3.190136	0.000820	0.004590	15	3.190136	0.000820	0.004590	15	11.	Choline (Cho)
5.220345	0.000829	0.424418	1387	5.220345	0.000829	0.424419	1387	5.220345	0.000829	0.424419	1387	12.	Glucose (Glc)

Padé-reconstructed data from a synthesized FID reminiscent of in vitro MRS data as encoded from benign ovarian cyst fluid [52]. The reconstructed data are converged at N/16 = 64, where N = 1024 (when the peaks have not yet been identified, the missing spectral parameters are denoted as –)

Table 4 Reconstructed data at 3 signal lengths with 32, 64 and 128 FID points (data for malignant)

$N/32 = 32$				$N/16 = 64$				$N/8 = 128$				k	Metabolite assignment
Re (f_k) (ppm)	Im (f_k) (ppm)	$|d_k|$ (au)	Concentration (μmol/L)	Re (f_k) (ppm)	Im (f_k) (ppm)	$|d_k|$ (au)	Concentration (μmol/L)	Re (f_k) (ppm)	Im (f_k) (ppm)	$|d_k|$ (au)	Concentration (μmol/L)		
–	–	–	–	1.020219	0.000828	0.024174	79	1.020219	0.000828	0.024174	79	1.	Isoleucine (Iso)
1.039257	0.001406	0.148343	485	1.040048	0.000831	0.120869	395	1.040048	0.000831	0.120869	395	2.	Valine (Val)
–	–	–	–	1.330124	0.000832	0.075887	248	1.330124	0.000832	0.075887	248	3.	Threonine (Thr)
1.409062	0.001372	2.046372	6688	1.410235	0.000838	2.000000	6536	1.410235	0.000838	2.000000	6536	4.	Lactate (Lac)
1.446902	0.008300	0.196825	643	1.510318	0.000834	0.179315	586	1.510318	0.000834	0.179315	586	5.	Alanine (Ala)
1.712040	0.004160	0.174575	571	1.720125	0.000833	0.149939	490	1.720125	0.000833	0.149939	490	6.	Lysine (Lys)
2.101571	0.031100	0.028695	94	2.130246	0.000829	0.018972	62	2.130246	0.000829	0.018972	62	7.	Methionine (Met)
2.470096	0.000838	0.251929	823	2.470118	0.000835	0.253366	828	2.470118	0.000835	0.253366	828	8.	Glutamine (Gln)
3.069840	0.003200	0.028376	93	3.050039	0.000832	0.020196	66	3.050039	0.000832	0.020196	66	9.	Creatine (Cr)
3.165277	0.003440	0.028617	94	3.130227	0.000831	0.024174	79	3.130227	0.000831	0.024174	79	10.	Creatinine (Crm)
–	–	–	–	3.190136	0.000830	0.012852	42	3.190136	0.000830	0.012852	42	11.	Choline (Cho)
5.220345	0.000839	0.079557	260	5.220345	0.000839	0.079559	260	5.220345	0.000839	0.079559	260	12.	Glucose (Glc)

Padé-reconstructed data from a synthesized FID reminiscent of in vitro MRS data as encoded from malignant ovarian cyst fluid [52]. The reconstructed data are converged at $N/16 = 64$, where $N = 1024$ (when the peaks have not yet been identified, the missing spectral parameters are denoted as –)

with $N/32 = 32$ signal points, nine of the twelve peaks were identified. For both the benign and the malignant cases isoleucine and threonine were undetected at $N/32$. Only one peak was identified in the region between 3.07 and 5.22 ppm at the signal length of $N/32 = 32$, and the position was slightly different for the benign and malignant case (3.14 and 3.17 ppm, respectively). For none of these peaks were all the spectral parameters exact to the input six decimal places of accuracy, neither for the data corresponding to the benign nor in the malignant cases, at $N/32$. On the middle set of columns of Tables 3 and 4, we see that in both of these cases, convergence was achieved. This is with $N/16 = 64$ signal points, where the FPT succeeded in reconstructing *exactly* (to six decimal places) all the spectral parameters of each of the twelve peaks corresponding to the input data for both the benign and the malignant cases. In other words, at the signal length $N/16 = 64$ all the reconstructed parameters are identical to the input data from Tables 1 and 2, respectively. The right set of columns from Tables 3 and 4 respectively, reveal that the convergence is stable with an increased number of signal points. Namely at $N/8 = 128$, all of the spectral parameters remain identical to those at $N/16 = 64$. At even longer fractions N/M ($M < 8$) of the full FID including $N = 1024$ ($M = 1$), we have verified that all the peak parameters reconstructed by the FPT remained unchanged in accordance with the concept of Froissart doublets (pole-zero cancellations).

2.2.2 Absorption spectra

As mentioned earlier, the diagonal Padé non-parametric estimation is presently achieved by evaluating the quotient spectrum P_K/Q_K. This is done without searching for any of the spectral parameters, unlike other parametric estimators (e.g., the HLSVD) that compute the envelope spectrum by first reconstructing the peak parameters $\{\omega_k, d_k\}$. The spectra in the FPT are presented in the absorption mode, which is defined as the real part of the corresponding complex mode. Hereafter, "absorption spectrum" will be used as the abridged nomenclature for "absorption total shape spectrum" in the terminology of sub-Sect. 1.1.2.3.

Here, we examine the convergence behavior of the FPT at the same signal lengths as used in the previous sub-Sect. (2.2.1) to confirm that the parameters' convergence naturally implies convergence of the corresponding absorption spectra. For comparison, the absorption spectra at the corresponding signal lengths from the familiar non-parametric method, the FFT are also shown.

Figure 1 displays the convergence of the absorption spectra at varying signal lengths for the FID which simulates the benign ovarian cyst data. The left three panels present the absorption spectra of the FFT at $N/32 = 32$ (top (i)), $N/16 = 64$ (middle (ii)) and $N/8 = 128$ (bottom (iii)). At each of these signal lengths, the FFT-generated spectra are rough and uninterpretable.

The right three panels of Fig. 1 show that the convergence of the FPT-generated spectra is consistent with the parametric data from Table 1. In the upper right hand panel (iv), nine of the twelve metabolites are detected. The remaining three resonances: isoleucine, threonine and the second resonance in the region between 3.1 and 3.2 ppm require 64 signal points to be resolved. At this latter signal length, all the peak heights are correct. Again, in agreement with Table 1, at $N/16 = 64$ the absorption spectrum
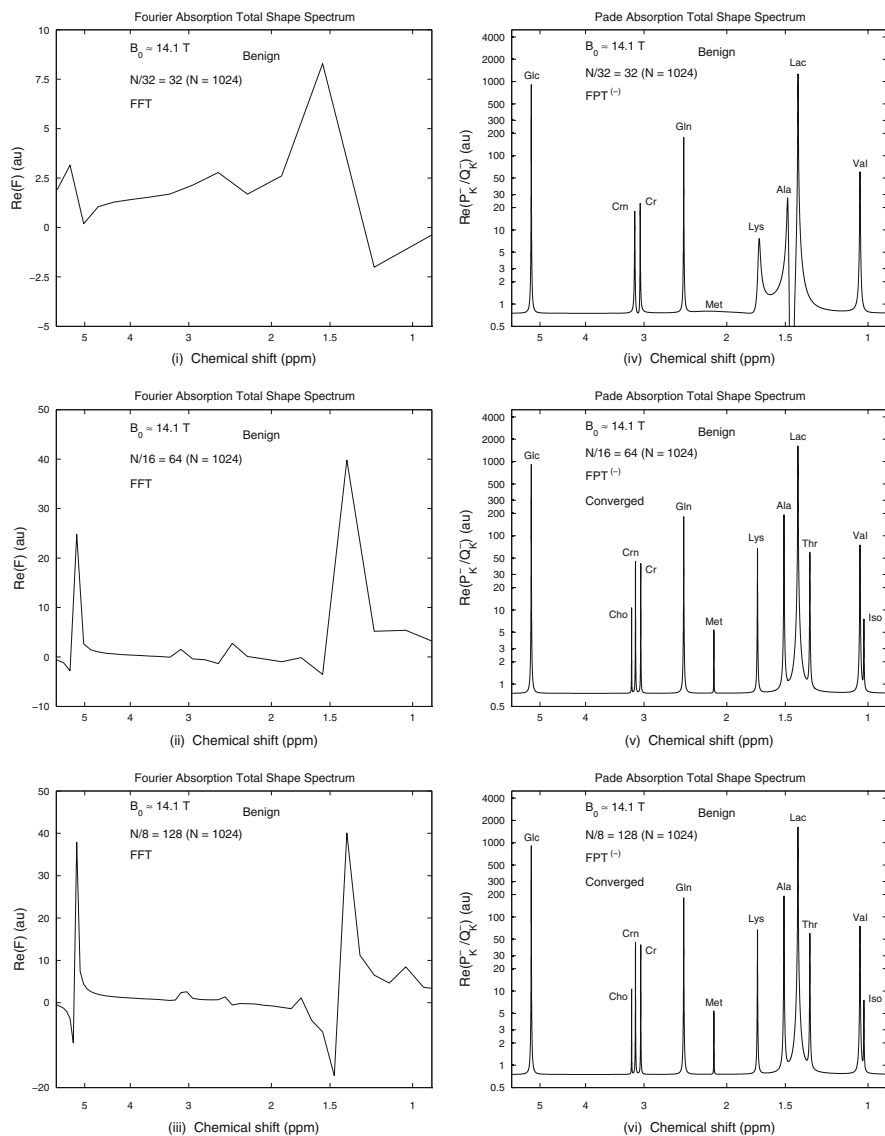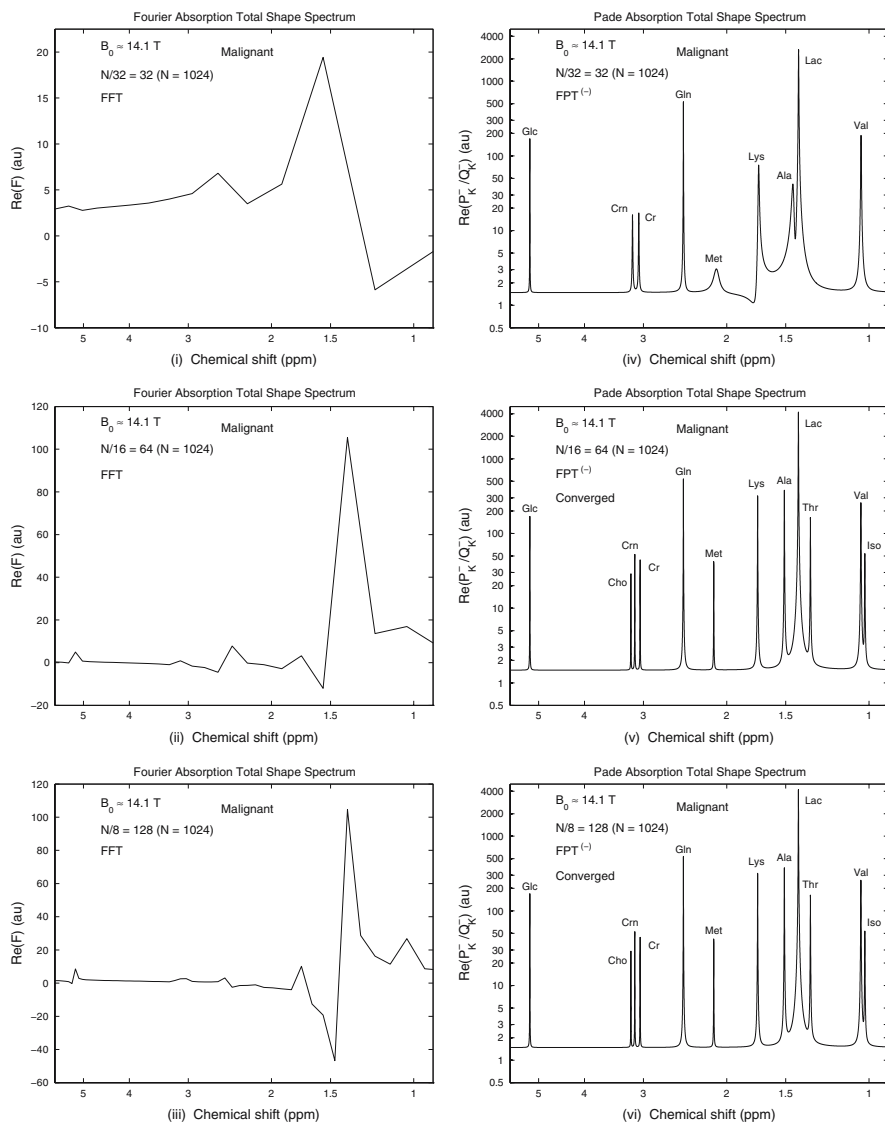
Fig. 1 Convergence of absorption total shape spectra (Benign); FFT (Left), FPT$^{(-)}$ (Right); FID lengths: N/M, $N = 1024$, $M = 8$–32

is fully converged in the FPT and remains so at the signal length of $N/8 = 128$. We have also verified that at even longer fractions N/M ($M < 8$) of the full FID including $N = 1024$ ($M = 1$), the spectra reconstructed by the FPT remained unchanged, as dictated by Froissart doublets.

The absorption spectra at varying signal lengths for the FID which simulates the malignant ovarian cyst data are shown in Fig. 2. The absorption spectra of the FFT (left panel) at $N/32 = 32$ (top (i)), $N/16 = 64$ (middle (ii)) and $N/8 = 128$ (bottom (iii)) are also rough and uninterpretable, as seen for the benign case.

Fig. 2 Convergence of absorption total shape spectra (Malignant); FFT (Left), FPT$^{(-)}$ (Right); FID lengths: N/M, $N = 1024$, $M = 8-32$

The convergence pattern of the FPT-generated spectra (right panel of Fig. 2) is consistent with the parametric data from Table 2. Specifically, at $N/32 = 32$ (top, (iv)), nine of the twelve metabolites are detected. Similarly to Fig. 1, the remaining three resonances (isoleucine, threonine and the second resonance in the region between 3.1 and 3.2 ppm) require 64 signal points to be resolved on Fig. 2. At $N/16 = 64$, all 12 metabolites are seen and they show the correct peak heights, such that the absorption spectrum is fully converged in the FPT (middle panel (v) as well as for the longer
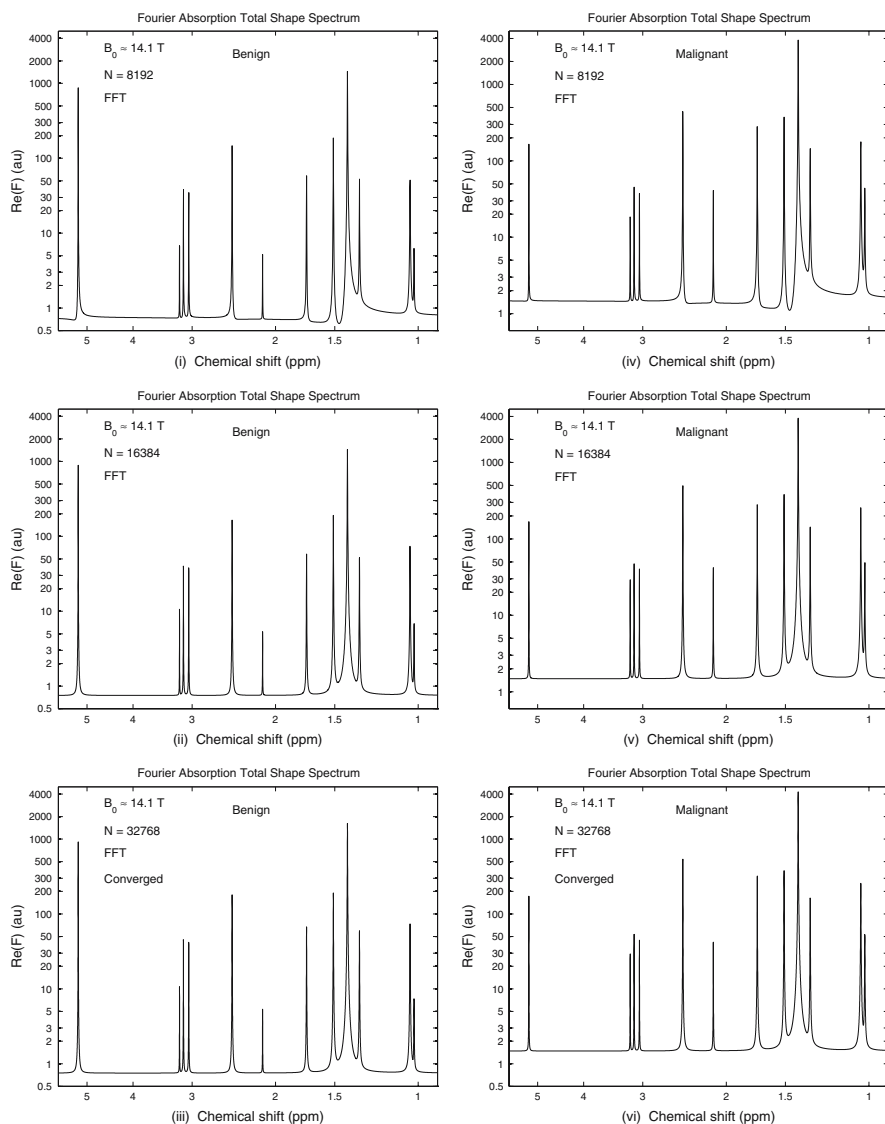
Fig. 3 Convergence of absorption total shape spectra in FFT at three long total acquisition times benign (Left), malignant (Right); FID lengths: $N = 8K = 8192$, $16K = 16384$, $32K = 32768$ (K = 1024)

signal length of $N/8 = 128$ (bottom panel (vi)). Again, we confirmed that at even longer fractions N/M ($M < 8$) of the full FID including $N = 1,024$ ($M = 1$), the spectra reconstructed by the FPT remained unchanged, in accordance with pole-zero cancellations.

Figure 3 depicts the convergence pattern of the absorption spectra in the FFT at three large signal lengths ($N = 8K = 8192$, $16K = 16384$, $32K = 32768$) where, as before, K denotes the kilobyte (K= 1024). Benign and malignant data are shown on

the left and the right column of Fig. 3, respectively. For both benign and malignant cases, the first FID length for which the positive-definite Fourier absorption spectra are obtained is very high, $N = 8K$ (top panels (i) and (iv)). All the 12 resonances are seen to be resolved in the FFT at $N = 8K$ on panels (i) and (iv), but several peak heights are incorrect. This implies that some of the metabolite concentrations estimated from the Fourier spectra by either fitting or peak integrations will be insufficiently accurate even at $N = 8K$. Moreover, it is obvious from panels (i) and (iv) at $N = 8K$ that there are significant baseline distortions for both benign and malignant cases. Such distortions would invalidate both fitting and numerical peak integrations. These baseline distortions disappear at $N = 16K$ on the middle panels (ii) and (v), but some of the peaks still have not reached their correct heights. Eventually, the FFT is found to converge at $N = 32K$ on the bottom panels (iii) and (vi) of Fig. 3. Nevertheless, it should be re-emphasized that this Fourier convergence is concerned only with the line-shapes from panels (i)–(vi), and not with quantification, which in this methodology necessitates post-processing via fittings or peak integrations that are ambiguous especially when spectral crowding occurs. All the quoted signal lengths in the FFT have been doubled by zero filling.

Figure 4 summarizes the convergence behavior of the FPT for the absorption spectra corresponding to data of benign (left panels) versus malignant ovarian cysts (right panels) at the signal lengths of $N/32 = 32$ (top panels, (i) and (iv)), $N/16 = 64$ (middle panels, (ii) and (v)), and $N/8 = 128$ (bottom panels, (iii) and (vi)). Once convergence has been achieved at $N/16 = 64$, notable differences can be observed in peaks heights between the benign and the malignant cases. The choline, glutamine, methionine, lysine, alanine, lactate, threonine, valine and isoleucine peaks are all higher in the malignant case, whereas the peak corresponding to glucose is higher in the benign case.

2.2.3 Metabolite maps of concentrations

We also studied the convergence pattern of the concentrations of the metabolites. In Fig. 5, the chemical shift is presented along the abscissae of the six panels, with concentrations as the ordinates. The input data are represented by the symbol "x", while the Padé-reconstructed data are shown as open circles. The data corresponding to the benign and malignant cases are presented in the left and right panels, respectively. Prior to convergence, at $N/32 = 32$ (top panels (i) and (iv)), the only metabolite for which the correct concentrations in both cases were obtained is glucose at 5.22 ppm (1387 μmol/L (benign) and 260 μmol/L (malignant), respectively). At $N/16 = 64$ (middle panels (ii) and (v)) and $N/8 = 128$ (bottom panels (iii) and (vi)), all of the metabolite concentrations are correct, as seen both numerically and by the graphic representation. For $N/16$ and $N/8$, this means that the "x's" are completely centered within the open circles, indicating full agreement between the input and reconstructed data (see also Tables 1–4).

Finally, Fig. 6 recapitulates the absorption spectra and the retrieved concentrations with the full convergence achieved by the FPT using only 64 FID points out of 1024 data sampled in the time domain. This combined plot illustrates the overall power of the FPT which performs shape estimation and quantification on the same footing without
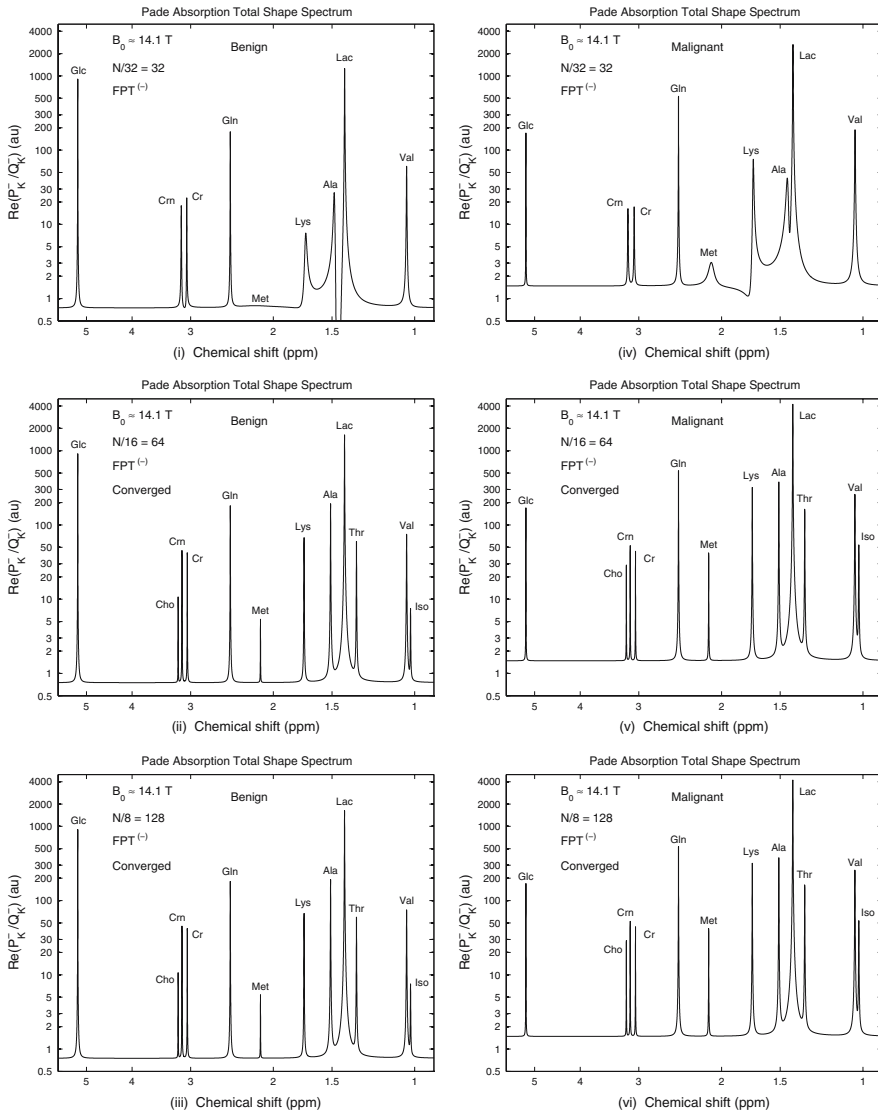
Fig. 4 Convergence of absorption total shape spectra in FPT$^{(-)}$; benign (Left), malignant (Right); FID lengths: N/M, $N = 1024$, $M = 8-32$

any post-processing and with no reliance upon other estimators. Fig. 6 is deemed to be most helpful for clinicians, since it gives both a graphic and a quantitative overview of MRS. Such a procedure is depicted on Fig. 6 as a comprehensive summary of signal processing, encompassing line-shape estimation and quantification, which culminates in the reconstructed concentrations as the diagnostically most relevant information from the examined tissue.
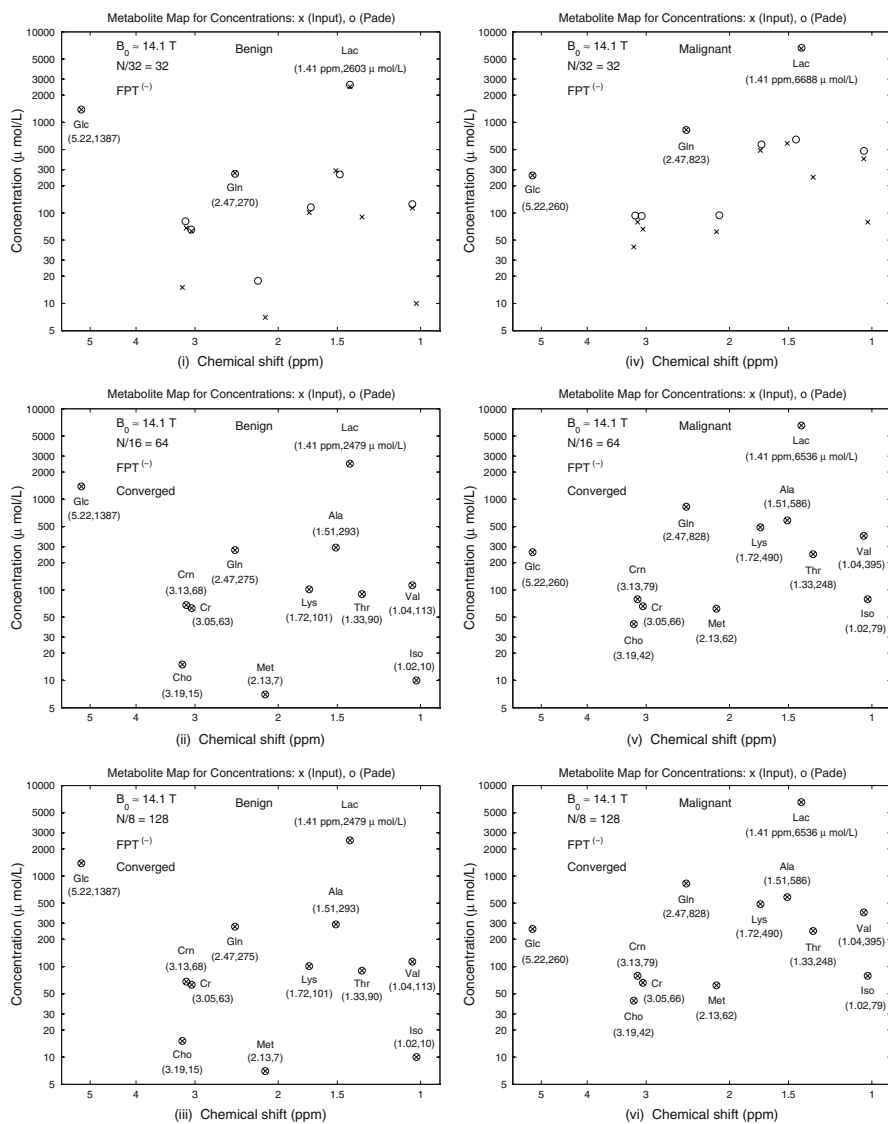
Fig. 5 Convergence of concentrations of metabolites in FPT$^{(-)}$; benign (Left), malignant (Right); FID lengths: N/M, $N = 1024$, $M = 8-32$

3 Discussion

The present work extends and elaborates the initial study [55] applying the fast Padé transform to MR data from benign and malignant ovarian cyst fluid. The powerful extrapolation features of the FPT are clearly demonstrated in that with only 64 data points, the Padé absorption spectra are fully converged, including a clear delineation of closely lying resonances such as alanine, lactate and threonine in the region between
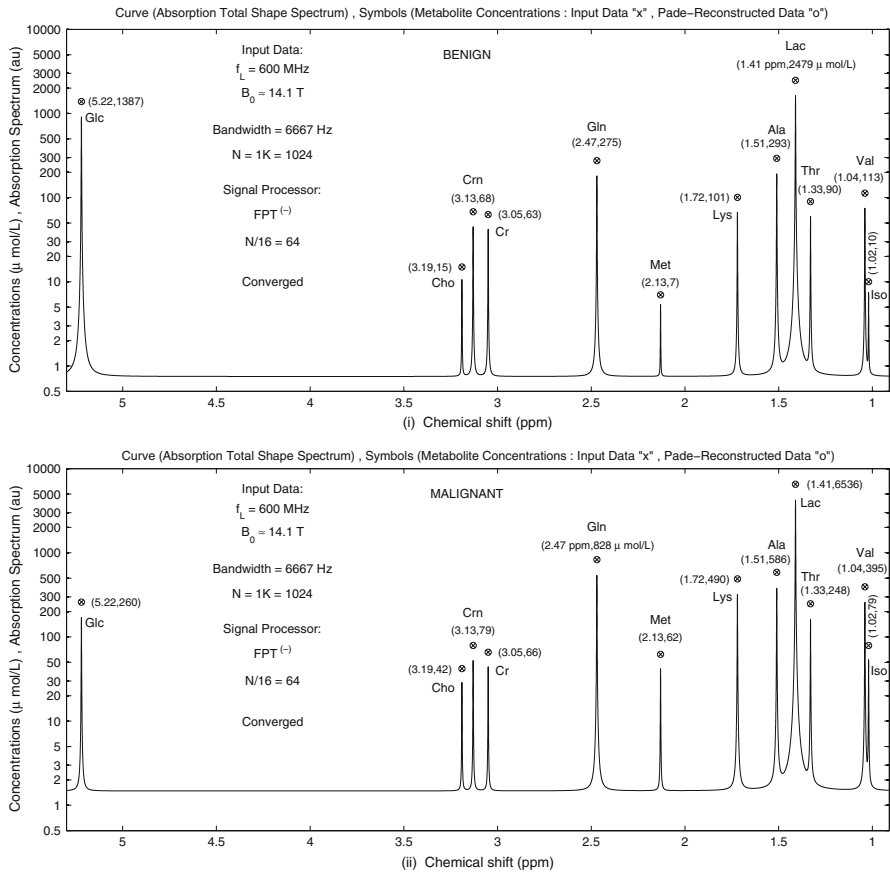
Fig. 6 Exact reconstruction of metabolite concentrations by FPT$^{(-)}$ using only 64 FID points from $N = 1024$: benign (Top), malignant (Bottom)

1.3 ppm and 1.51 ppm, and even the nearly overlapping isoleucine and valine which are separated by only 0.02 ppm. In marked contrast, the FFT yielded entirely uninterpretable spectra at these short signal lengths. As reviewed in Sect. 1.1.1, the envelopes of MR time signals decay exponentially such that the signal intensity is the highest early in the encoding. It is thus advantageous to encode the time signal as rapidly as possible, i.e., to avoid long T when mainly noise will be measured. This is particularly important for clinical signals encoded at lower magnetic field strengths.

The FPT provides not only the shape spectra, but also the vitally important parametric analysis (quantification) from which the metabolite concentrations are obtained. In the present problem, with only 64 data points out of 1024 sampled data, the FPT exactly reconstructed all the spectral parameters to an accuracy of six decimal places for all the twelve metabolite peaks. These parameters were then used to compute metabolite concentrations simply and unequivocally. With the standard Fourier approach, metabolite concentrations are estimated from the shape spectra by integrating the areas under the peaks or fitting the peaks to a subjectively chosen number of

Lorentzians and/or Gaussians. Even for clearly delineated peaks, as noted, this procedure of numerical quadrature is vulnerable to subjectivity due to the uncertainty about the lower and upper integration limits. However, when the peaks overlap, this standard method for reconstructing metabolite concentrations is fraught with major difficulties and uncertainties; it is thus well-recognized that "spectral crowding" creates quantification problems [54]. This "spectral crowding" problem does not obstruct the FPT, which via parametric analysis, yields reliable information about the concentrations not only of isolated resonances, but also of those that are overlapping [10,11].

As reviewed in Sect. 1.2.2, a substantial number of MR-observable compounds have been found to provide some distinction between benign and cancerous ovarian lesions [48–51] when in vitro MRS is applied using high magnetic field strength and the conventional laboratory specimen processing techniques. Notably, concentrations of adjacent resonances such as threonine (1.33 ppm), lactate (1.41 ppm) and alanine (1.51 ppm) and the nearly overlapping resonances isoleucine and valine in the region of 1.02 to 1.04 ppm differ significantly in these two types of lesions [51]. The high concentrations of these branched chain amino acids are seen as protein breakdown products due to necrosis and proteolysis. However, none of these studies reported any metabolite alone or in combination with other metabolites which unequivocally distinguished benign from cancerous ovaries. Even when the differences in concentrations were statistically highly significant such as in Ref. [51], the ranges were not distinct. One avenue for further investigation which is currently underway is to apply the FPT to larger-scale in vitro experimental MRS data from benign and malignant ovarian lesions. In this way, we are exploring the possibilities of whether the FPT with its capacity to unequivocally yield exact quantifications could also specify metabolite concentrations that more clearly distinguish cancerous from non-neoplastic ovary. The FPT could thereby help establish the standards of MR-detectable metabolite concentrations for normal versus specific pathological entities of the ovary.

The high resolution of the FPT also could be of benefit for in vivo MRS investigations, for which, as reviewed in Sect. 1.2.1, poor SNR has been a major obstacle which hampered progress in ovarian cancer diagnostics via MRS. It has been suggested that in vivo MRS could become the method of choice for accurate detection of early stage ovarian cancer, insofar as the current obstacles hindering the acquisition of high quality time signals and the subsequent reliable analysis of spectra as well as their interpretation can be surmounted [50]. The results of the present study suggest that application of the FPT could be a step towards realizing this goal, especially if in vitro and in vivo clinical correlations together with histopathology were initially provided for verification. On a practical level, the metabolite concentration maps that we presently initiated could be a particularly useful tool for clinicians to facilitate reliable interpretation.

The present study uses noise-free FIDs, since we wanted to set up the fully-controlled standard for the FPT in the case of the initial application of this method to data within the realm of ovarian cancer diagnostics by MRS. This is methodologically justified [10]. The next steps will be to extend our analysis to both noise-corrupted synthesized data (still well-controlled) and to encoded FIDs such as those from Ref. [51]. These studies are on-going and the results, including *doublet and multiplet resonances* will be reported shortly.

4 Conclusion

The capacity of the fast Padé transform to resolve and precisely quantify all the physical resonances as encountered in benign versus malignant ovarian cystic fluids is clearly demonstrated in the present study. This Padé–based quantification as a parametric estimation is achieved with a very small number of signal points. The practical significance of such findings is in the avoidance of the time signals' exponential tail which is embedded in the background, and, thus, causes severe problems in quantification. Without any fitting or numerical integration of peak areas, the fast Padé transform reliably and unequivocally yields the metabolite concentrations of major importance for distinguishing benign from malignant ovarian lesions. These features of the FPT should be of benefit for ovarian cancer diagnostics via MRS. Such an avenue is of clinical urgency for early ovarian cancer detection, a goal which is still elusive and achievement of which would confer a major survival benefit.

References

1. Dž. Belkić, K. Belkić, J. Math. Chem. in press, (2007)
2. Dž. Belkić, *Quantum mechanical signal processing and spectral analysis* (Institute of Physics Publishing, Bristol, UK, 2004)
3. Dž. Belkić, K. Belkić, Phys. Med. Biol. **50**, 4385 (2005)
4. P.A. Bottomley, J. Magn. Reson. Imaging **2**, 1 (1992)
5. Y.-D. Cho, G.-H. Choi, S.-P. Lee, J.-K. Kim, Magn. Reson. Imaging **21**, 663 (2003)
6. K.S. Opstad, S.W. Provencher, B.A. Bell, J.R. Griffiths, F.A. Howe, Magn. Reson. Med. **49**, 632 (2003)
7. Dž. Belkić, Nucl. Instrum. Methods Phys. Res. **A 525**, 366 (2004)
8. W.W.F. Pijnappel, A. van den Boogaart, R. De Beer, D. van Ormondt, J. Magn. Reson. **97**, 122 (1992)
9. Dž. Belkić, Nucl. Instrum. Methods Phys. Res. **A 525**, 372 (2004)
10. Dž. Belkić, Phys. Med. Biol. **51**, 2633 (2006)
11. Dž. Belkić, Phys. Med. Biol. **51**, 6483 (2006)
12. Dž. Belkić, Adv. Quant. Chem. **51**, 157 (2006)
13. Dž. Belkić, P.A. Dando, H.S. Taylor, J. Main, Chem. Phys. Lett. **315**, 135 (1999)
14. Dž. Belkić, P.A. Dando, J. Main, H.S. Taylor, J. Chem. Phys. **113**, 6542 (2000)
15. Dž. Belkić, P.A. Dando, H.S. Taylor, J. Main J, S-K. Shin, J. Phys. Chem. **A 104**, 11677 (2000)
16. M. Deschamps, I. Burghardt, C. Derouet, G. Bodenhausen, Dž. Belkić, J. Chem. Phys. **113**, 1630 (2000)
17. J. Main, P.A. Dando, Dž. Belkić, H.S. Taylor, Europhys. Lett. **48**, 250 (1999)
18. J. Main, P.A. Dando, Dž. Belkić, H.S. Taylor, J. Phys. **A 33**, 1247 (2000)
19. J. Pfeuffer, I. Tkáč, S.W. Provencher, R. Gruetter, J. Magn. Reson. **141**, 104 (1999)
20. Dž. Belkić, Nucl. Instrum. Methods Phys. Res. **A 525**, 379 (2004)
21. Dž. Belkić, K. Belkić, Int. J. Quantum Chem. **105**, 493 (2005)
22. S. Pecorelli, G. Favalli, L. Zigliani, F. Odicino, Int. J. Gynaecol. Obstet. **82**, 369 (2003)
23. M.A. Brewer, K. Johnson, M. Follen, D. Gershenson, R. Bast, Clin. Cancer Res **9**, 20 (2003)
24. I.B. Runnebaum, E. Stickeler, J. Cancer Res. Clin. Oncol. **127**, 73 (2001)
25. M.M. Fields, E. Chevlen, Clin. J. Oncol. Nurs. **10**, 77 (2006)
26. S. Bhoola, W.J. Hoskins, Obstet. Gynecol. **107**, 1399 (2006)
27. N. Einhorn, R. Bast, R. Knapp, B. Nilsson, V. Zurawski, K. Sjövall, Gynecol. Oncol. **79**, 466 (2000)
28. K. Belkić, *Molecular imaging through magnetic resonance for clinical oncology* (Cambridge, UK: Cambridge International Science Publishing, 2004)

29. M.J. Duffy, J.M. Bonfrer, J. Kulpa, G.J. Rustin, G. Soletormos, G.C. Torre, et al. Int. J. Gynecol. Cancer **15**, 679 (2005)
30. E.I.O. Garner, J. Reprod. Med. **50**, 447 (2005)
31. F. Kong, C. Nicole White, X. Xiao, Y. Feng, C. Xu, D. He, et al. Gynecol. Oncol. **100**, 247 (2006)
32. Y. Liu, Technol. Cancer Res. Treat. **5**, 61 (2006)
33. G. Mor, I. Visintin, Y. Lai, H. Zhao, P. Schwartz, T. Rutherford, et al. Proc. Natl. Acad. Sci. USA **102**, 7677 (2005)
34. A.V. Rapkiewicz, V. Espina, E.F. Petricoin, L.A. Liotta, Eur. J. Cancer **40**, 2604 (2004)
35. D.F. Ransohoff, J. Natl. Cancer Inst. **97**, 315 (2005)
36. S.S. Buys, E. Partridge, M.H. Greene, P.C. Prorok, D. Reding, T.L. Riley et al. Am. J. Obstet. Gynecol. **193**, 1630 (2005)
37. K.L. Taylor, R. Shelby, E. Gelmann, C. McGuire, J. Natl. Cancer Inst. **96**, 1083 (2004)
38. U.S. Preventive Services Task Force, Ann. Fam. Med. **2**, 260 (2004)
39. I. Imaoka, A. Wada, K. Kaji, T. Hayashi, M. Hayashi, M. Matsuo, K. Sugimura, Radiographics **26**, 1431 (2006)
40. J.A. Spencer, Br. J. Radiol. **78**, S94 (2005)
41. K. Kinkel, Y. Lu, A. Mehdizade, M-F. Pelte, H. Hricak, Radiology **236**, 85 (2005)
42. S. Harlap, S.H. Olson, R.R. Barakat, T.A. Caputo, S. Forment S, A.J. Jacobs, et al. Ann. Epidemiol. **12**, 426 (2002)
43. D.A. Hill, S. Preston-Martin, R.K. Ross, L. Bernstein, Cancer Causes Control **13**, 711 (2002)
44. L.A. Brandão, R.C. Domingues, *MR spectroscopy of the brain* (Philadelphia, PA: Lippincott Williams & Wilkins, 2004)
45. S.W. Cho, S.G. Cho, J.H. Lee, H.-J. Kim, M.H. Lim, J.H. Kim, C.H. Suh, Korean J. Radiol. **3**, 105 (2002)
46. S. Hascalik, O. Celik, G. Erdem, Int. J. Gynecol. Obstet. **90**, 152 (2005)
47. S. Hascalik, O. Celik, K. Sarak, M.M. Meydanli, A. Alkan, B. Mizrak, Gynecol. Obstet. Invest. **60**, 121 (2005)
48. T. Okada, M. Harada, K. Matsuzaki, H. Nishitani, T.J. Aono, Magn. Reson. Imaging **13**, 912 (2001)
49. I.C. Smith, D.E. Blandford, Biochem. Cell. Biol. **76**, 472 (1998)
50. J.C. Wallace, G.P. Raaphorst, R.L. Somorjai, C.E. Ng, M. Fung Kee Fung, M. Senterman, I.C. Smith, Magn. Reson. Med. **38**, 569 (1997)
51. L.F.A.G. Massuger, P.B.J. van Vierzen, U. Engelke, A. Heerschap, R. Wevers, Cancer **82**, 1726 (1998)
52. E.A. Boss, S.H. Moolenaar, L.F. Massuger, H. Boonstra, U.F. Engelke, J.G. de Jong, R.A. Wevers, NMR Biomed. **13**, 297 (2000)
53. C.E. Mountford, S. Doran, C.L. Lean, P.L. Russell, Chem. Rev. **104**, 3677 (2004)
54. L. Gluch, ANZ. J. Surg. **75**, 464 (2005)
55. J.K. Nicholson, I.D. Wilson, Prog. NMR Spectrosc. **21**, 1245 (1989)
56. K. Belkić, Nucl. Instrum. Methods Phys. Res. A, in press, (2007)